IET Journals

IET Electric Power Applications

Analysis of perforated magnetic shields for electric power applications

P. Sergeant[1,*]   R.V. Sabariego[2]   G. Crevecoeur[1]   L. Dupré[1]
C. Geuzaine[2]

[1]Department of Electrical Energy, Systems and Automation, Ghent University, Sint-Pietersnieuwstraat 41, B-9000 Ghent, Belgium
[2]Department of Electrical Engineering and Computer Science (ACE), University of Liège, Sart Tilman Campus, Grande Traverse, 10 (B28), B-4000 Liège, Belgium
*Department of Electrotechnology, Faculty of Applied Engineering Sciences, University College Ghent, Schoonmeersstraat 52, B-9000 Ghent, Belgium
E-mail: peter.sergeant@ugent.be

Abstract: The shielding performance of perforated magnetic shields for electric power applications is described. The shielding of an axisymmetric induction heating device is studied as a function of frequency, number of perforations and dimensions of the perforations. From the numerical point of view, the perforations cause the numerical model to be 3D. A numerical optimisation is carried out to find the optimal geometry with respect to the shielding factor and the volume of the shield. For the optimisation, two approaches are presented. The first approach is fast and easy-to-implement, but has limited accuracy. It uses a classical 2D axisymmetric model where the perforations are approximated by 'axisymmetric air gaps' resulting in a segmented shield. It is shown how to modify the 2D model to obtain results that are similar to the ones of a 3D model. The second approach is more accurate although quite fast, but more difficult to implement. It combines a 3D thin-shell finite element model with the unmodified 2D model in a space mapping optimisation algorithm. The validation of both models is based on experimental work for an unperforated shield and for the optimised perforated shield.

1 Introduction

In recent literature, many papers about shielding have been published in low frequency – i.e. for quasi-static applications where the studied device is much smaller than the electromagnetic wavelength [1]. These shields are generally unperforated metallic sheets. However, in practice, shields often contain holes to guide control or power wires or to obtain sufficient cooling. In [2], perforated shields are studied using the 2D finite element method (FEM). In this study, the influence of frequency, orientation of the gaps (parallel or perpendicular to the field), size and number of the gaps are studied, and it gives a good insight into 2D perforated shield problems. In [3], the effect on the shielding performance of a single hole of an electrical steel sheet is investigated. Because the study focusses on the effect

of material degradation near the hole edge, the authors could choose a set-up with only one hole. This makes it possible to use a 2D axisymmetric FEM, with a non-linear constitutive law.

Furthermore, there is a need to study perforated shields for a variety of industrial applications up to 1 MHz frequency. Such a study usually requires a 3D numerical model. Even if the device to shield can be described by a 2D axisymmetric or planar model, the introduction of perforations in the shield often creates geometrical variations in the azimuthal direction or, in case of a planar problem, in the direction perpendicular to the modelled plane. Analytical expressions of shields with holes exist for simple shield and source geometries [4], but not for the majority of the applications in industry. As a result, in

most cases, the shielded application has to be modelled by a 3D numerical model.

The design of a shield requires many evaluations of the 3D numerical model, as parametric studies or optimisations have to be carried out. The computation time may become huge when using classical optimisation techniques (e.g. gradient algorithm, Nelder–Mead Simplex, genetic algorithm, . . .) in combination with a classical 3D FEM that usually generates a very dense mesh in thin structures such as the shield.

To study 3D shielding configurations efficiently, the typical computational burden of the 3D FEM should be minimised. We present two methods.

The first method is a practical approach. It is easy to implement, does not require much CPU time, but its results may have limited accuracy. It is based on a conventional 2D model that is slightly modified to better approach the results of the 3D model. It is further denoted as 'modified 2D-model'. Because it does not use advanced techniques for numerical models or optimisation, this approach is useful for a quick, approximate design of a perforated shield for a given application.

The second method is a more scientific approach. This approach is also fast in comparison with the conventional optimisation of a classical 3D model. However, in contrast with Method 1, it is also accurate. Therefore it uses a 3D FEM with a computationally efficient thin-shell approximation. Furthermore, it combines the original (unmodified) 2D FEM with the 3D FEM in a space mapping optimisation algorithm [5, 6]. The algorithm optimises the geometry of the 3D FEM fast, because it predominantly evaluates the computationally less demanding 2D FEM. Method 2 is useful to study perforated shields

precisely, but requires the effort to program non-standard numerical models and optimisation routines.

The study aims at providing accurate information about perforated shields for a given application and numerical tools to design and study perforated shields for other potential applications.

The paper is organised as follows. In Section 2, the three finite element models used are described: the unmodified 2D FEM and the 3D FEM with thin-shell approximation, both used in Method 2, and the modified 2D FEM used in Method 1. In the same section, these models are validated by comparing their field predictions with each other and with measurements. Then, the first optimisation method using the modified 2D FEM is described in Section 3. Finally, the optimisation based oncombining a 2D FEM and 3D FEM is explained in detail in Section 4.

2 2D and 3D finite element models for the induction heating application

2.1 Application

Fig. 1 shows the geometry and a picture of the studied induction heating application. The shield is an axisymmetric ring with circular perforations of diameter d. There are n perforations aligned in axial direction, repeated periodicallyalong the circumference. Obviously, when considering the perforations, the originally axisymmetric shield cannot be modelled in 2D anymore. In the axial direction, the spaces b between adjacent holes or between a hole and the shield edge are equal. For a given shield height h_p, b is defined as $b = (h_p - nd)/(n + 1)$. In the azimuthal direction (along the circumference), the space between
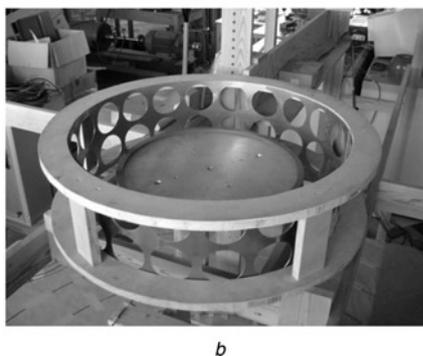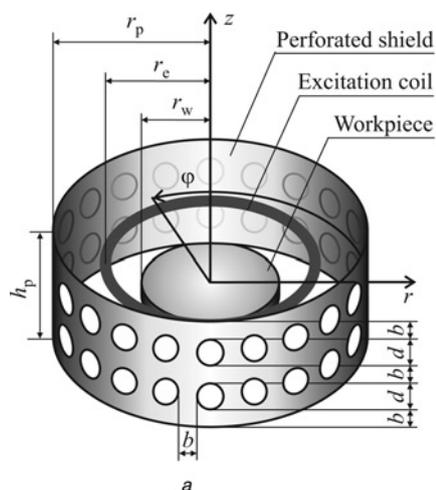
**Figure 1** *Geometry and a picture of the studied induction heating application*

a Geometry of the induction heating application and the perforated shield for $n = 2$. The values of the parameters can be found in Table 1
b Picture of the optimised shield with $d = 76$ mm and $n = 2$

adjacent holes is also b (approximately). Consequently, the number of holes along the circumference, n_h, is $2\pi r_p/(d + b)$ (approximately).

2.2 Unmodified 2D FEM and 3D FEM with thin-shell approximation

The 2D FEM is an axisymmetric, quasi-static, time-harmonic and linear model, using second-order Lagrange elements [7]. Because the $z = 0$ plane is a symmetry plane, only half of the geometry is modelled. The domain and the boundary conditions for the φ-component of the vector potential A_φ are shown in Fig. 2. The target region is the area where the field reduction is studied. This classical model uses a sufficiently large domain to avoid the influence of the boundaries on the magnetic quantities in the relevant regions. The shield region is meshed using classical elements: there are no impedance boundary conditions like in [8] nor is the shield modelled using thin-shell formulation [9]. Therefore this model can be created using almost any commercial FEM software package. The mesh density in the shield is chosen such that there are two layers of elements in the shield at low frequencies, where the penetration depth δ is much larger than half the shield thickness (for a frequency $f = 100$ Hz, $t_p/2 \ll \delta = 1.1$ mm). For higher frequencies where the penetration depth is much smaller than half the shield thickness (for a frequency $f = 10$ kHz, $t_p/2 \gg \delta = 0.11$ mm), the maximal size of the elements in the shield equals δ. The holes in the 2D shield model are represented by air gaps that split up the shield into several segments (see Fig. 2), similar to the perforated shield in [2]. The CPU time for the 2D FEM is 2.7 s. It has 11 000 unknowns if $t_p/2 \ll \delta$.
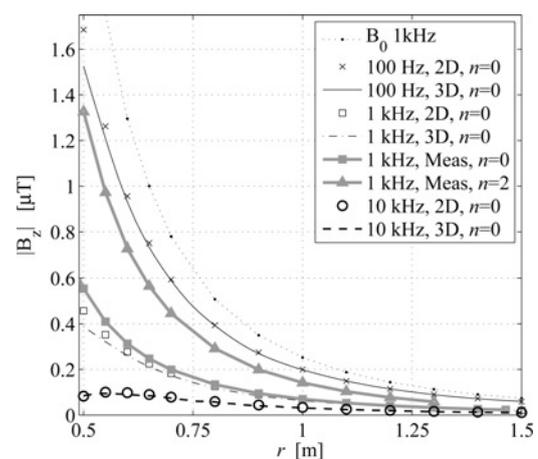
The 3D FEM uses a thin-shell approximation [9]: it reduces the thin-shell to an average surface situated halfway between the inner and the outer surface of the shell. It can be locally assumed that the electric and magnetic fields have no component perpendicular to the surface, which allows one to establish impedance boundary conditions. We adopt a magnetic vector potential formulation in which the
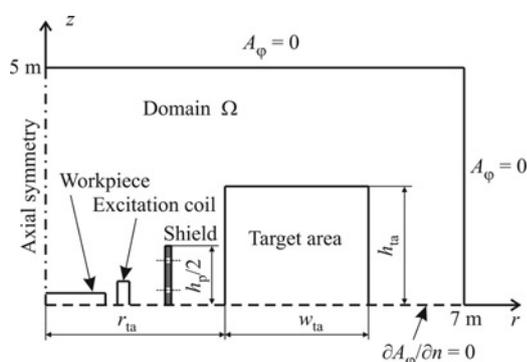
surface term is split into two terms that account for the continuous and discontinuous magnetic vector potential across the shield [9]. Further, the 3D model takes advantage of the symmetry with regard to the plane $z = 0$ and the symmetrical distribution of the holes. The CPU time is 26 s. It has 41 000 unknowns. When using a commercial software package that does not use the thin-shell formulation, the CPU time is more than double. All results indicated by '3D FEM' further in this paper are obtained by this 3D FEM with thin-shell approximation.

Both models use linear material properties. The constant permeability used in the linear FEM calculations is obtained from a measured hysteresis loop for an induction of 3 mT, which is a typical value of the average induction in the shield. As an extension, non-linear calculations are also possible wherein the permeability is an eighth-order polynomial function, obtained from several hysteresis loop measurements. In the latter case, the function is complex to represent hysteresis (phase shift between field and induction) like in [10]. It was verified for the considered induction heating application that when changing the shield geometry, the induction level does not change dramatically, so that the linear approximation is sufficiently accurate. However, for other applications, it should be verified if linearisation is acceptable. In [3], for example, Fig. 3 shows a rather small influence of the shielding as a function of the applied magnetic field: for an electrical steel M310-50A, the shielding factor improved by 30% maximally when increasing the field from 200 to 1600 A/m. For a grain-oriented M105-30P, the increase was about 17% when increasing the field between 200 and 1000 A/m. In [10] – considering a completely different cylindrical shielding configuration – the influence on the shielding

Figure 2 *Geometry of the 2D finite element model and boundary conditions for n = 4. The values of the parameters can be found in Table 1*

Figure 3 *|B_z(r)| in the z = 0 plane as a function of the position r for f = 100 Hz − 1 kHz − 10 kHz, obtained by unmodified 2D FEM, 3D FEM and measurements for an unperforated shield (n = 0) and a perforated shield (n = 2, d = 76 mm). B_0 is the induction obtained without shields*

125

© The Institution of Engineering and Technology 2009

was much larger: the shielding factor improved by a factor 5 when increasing the field from 4 to 400 A/m.

2.3 Validation of the unmodified 2D FEM and the 3D FEM with thin-shell approximation

The unmodified 2D and 3D models with thin-shell approximation differ in several ways: not only are the holes in the 2D model approximated by cylindrical air gaps, the 3D model also uses a thin-shell formulation, whereas the 2D model does not. Therefore in Fig. 3, the two models are compared with each other and also with the measurements for an axisymmetric geometry (unperforated shield: 2D and 3D geometry are equivalent) at three frequencies f: 100 Hz, where $t_p/2 \ll \delta$, 10 kHz, where $t_p/2 \gg \delta$ and 1 kHz. The figure shows the magnetic induction in the $z = 0$ plane of the target area.

At 100 Hz, the shielding is mainly established by flux shunting because of the high permeability of the shield, and by rather small eddy currents that are distributed almost uniformly along the shield width (no skin effect). The field reduction is rather poor and most effective very close to the shield.

At 10 kHz, the field reduction mechanism is dominated by induced currents, resulting in much more efficient shielding, also at larger distance from the shield. The difference in the field pattern can be seen in Fig. 4: at 100 Hz, the field lines are strongly attracted to the shield; at 10 kHz, a small part is still attracted – the shield is ferromagnetic – but most field lines are repelled into the region between the excitation coil and the shield.

At 1 kHz, Fig. 3 shows that both models correspond well with each other and with the measurements. Also at 1 kHz, the figure shows the induction of the perforated shield that has the optimised number of holes and optimised hole diameter in Section 4. Obviously, the holes deteriorate the

shielding considerably. Nevertheless, the perforated shield still mitigates the field despite of the big holes of 76 mm diameter: the shielding factor $s(r)$ – defined as the magnetic flux density in a point divided by the same quantity (B_0) in the same point without shield – is on average about 0.6 for the perforated shield and about 0.3 for the unperforated one.

By adding the shields, the magnetic stray field of the induction heater should comply with the reference levels of the ICNIRP [11] in the target area (between $r = 0.5$ m and $r = 1.5$ m). In the experiment, the excitation current was reduced by a factor 100 for practical reasons. To compare the obtained induction values with the ICNIRP reference at full power, the induction levels in Fig. 3 should be multiplied by 100. At 100 Hz, the ICNIRP reference level for occupational exposure to magnetic flux density is 250 μT. Without shield, the flux density exceeds this value in the target area. Fig. 3 shows that with the shield, the flux density rescaled by a factor 100 never exceeds the limit of 250 μT. For 1 kHz and 10 kHz, the ICNIRP limit is 30.7 μT. Without the shield, this limit is exceeded up to a radius of about 1 m. At $r = 0.5$ m, the field is about 10 times stronger than the limit. With the shield present, the flux density exceeds the limit slightly in the lower left corner ofthe target area (for $r < 0.6$ m) at 1 kHz. At 10 kHz, the flux density exceeds the ICNIRP limits nowhere in the target area.

For several numbers of holes with constant diameter, Fig. 5a shows the shielding factor $s(r)$ for the shield with properties in Table 1 and $f = 100$ Hz. For $n = 0$, the unmodified 2D and the 3D model with thin-shell approximation should yield identical results, but the figure shows that the curve from the 3D FEM (solid line) and the curve from the unmodified 2D FEM (cross-markers) are not exactly the same because of numerical inaccuracy. Notice, however, that the vertical scale is very detailed. Furthermore for $n > 0$, it can be seen that all curves of the 2D model (indicated by markers) are in the upper part of
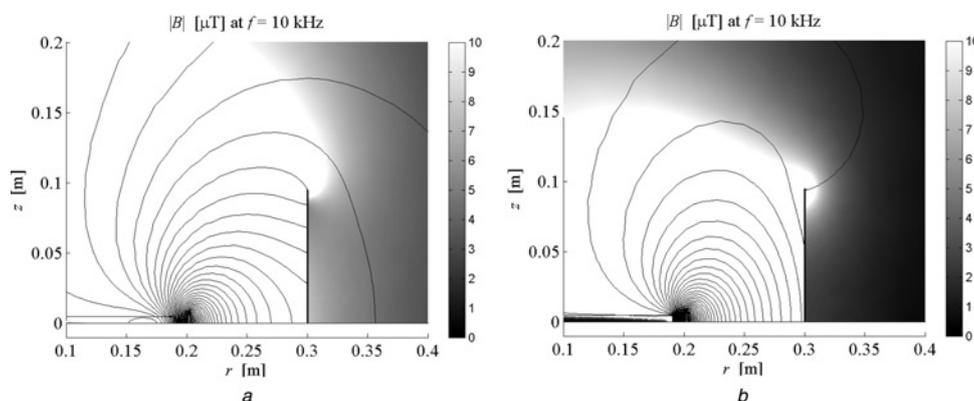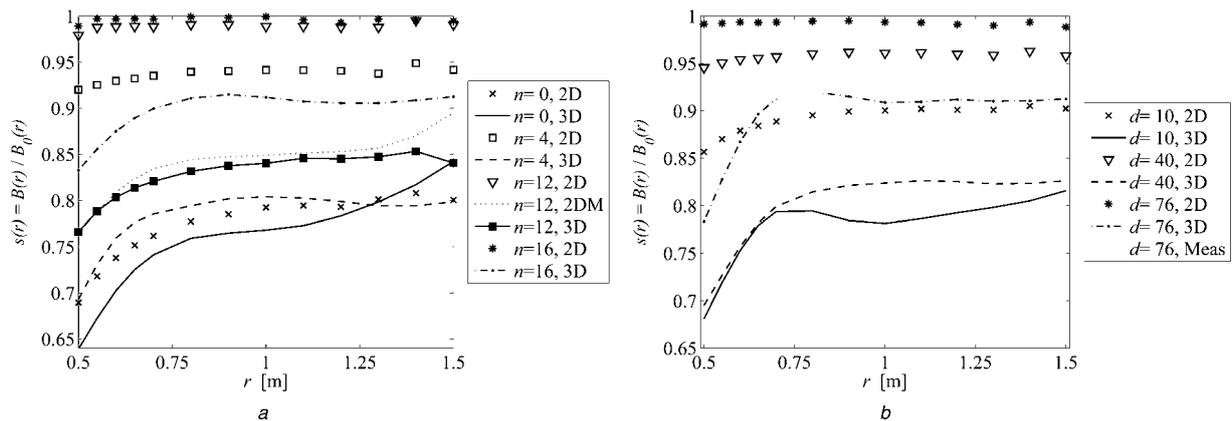

Figure 4 Magnetic flux density
a at $f = 100$ Hz, the field lines are attracted to the shield, thanks to its high permeability
b at $f = 10$ kHz, the field lines are repelled from the shield by induced currents

Figure 5 *For f = 100 Hz, shielding factor s(r) in the z = 0 plane*
a for several numbers of holes *n* with diameter 0.01 m
b for *n* = 2 holes with several hole diameters *d* in mm, as a function of the position *r* in the target area
The results are obtained by unmodified 2D FEM (2D), modified 2D FEM (2DM), 3D FEM and measurements. Experiments show that the dependence of s(r) on the azimuthal coordinate φ is negligible

the figure, which means that the predicted shielding efficiency is poor. It is clear that the unmodified 2D model is not able to predict well the shielding factor in case of perforations: it underestimates the shielding efficiency because the circumferential air gaps in the unmodified 2D model

Table 1 Geometrical and electromagnetic properties

Excitation	Inner radius	r_e	201.2 mm
	Cross-section width	w_e	1.5 mm
	Cross-section height	h_e	16.0 mm
	Current	l_e	40 A
	Frequency	f	(100−10 kHz)
Workpiece	Outer radius	r_w	191 mm
	Cross-section height	h_w	10.0 mm
	Conductivity	σ_w	3.7×10^7 S/m
	Permeability	μ_w	μ_0
Shield	Inner radius	r_p	300.0 mm
	Sheet thickness	t_p	0.65 mm
	Height	h_p	190 mm
	Hole diameter	d	$0-h_p$
	Number of holes	n	$0-n_{max}$
	Conductivity	σ_p	5.9×10^6 S/m
	Permeability	μ_p	$372\mu_0$
Target area	Inner radius	r_{ta}	0.50 m
	Cross-section width	w_{ta}	1.0 m
	Cross-section height	h_{ta}	0.8 m

act as flux barriers (for flux along the z-axis) that are not present in the 3D model that represents more faithfully the real application.

A similar conclusion can be drawn when changing the diameter *d* for a constant number of gaps (Fig. 5*b*). This figure also shows measurements for the shield with *n* = 2 and *d* = 76 mm. The measured s(r) is very close to the one simulated by the 3D FEM. The unmodified 2D FEM predicts an incorrect, very poor shielding factor.

At 10 kHz, Figs. 6*a* and 6*b* show similar plots as in Figs. 5*a* and 5*b* at 100 Hz. Again, we first compare the results of the 2D and 3D model for *n* = 0, where the results should be equal. The field in the target area is weak so that the relative difference between the two models is significant, although Fig. 3 shows that the absolute difference in fields is very small. For *n* > 0, the correspondence between 2D and 3D models is better than at 100 Hz. The shielding efficiency predicted by the 3D model is somewhat better because the 2D model underestimates the cross-section for the induced currents: it uses *b* as height, whereas in the 3D model, this height varies between *b* and *b* + *d*. The measured shielding factor corresponds well with the results of the 3D model in the region *r* < 0.7 m, close to the shield. It deviates up to 20% for *r* > 1.3 m, probably because the fields are so weak that the poor signal-to-noise ratio may reduce the accuracy of the measurement.

2.4 Modified 2D FEM

At low frequency, the shielding is caused by flux shunting in the ferromagnetic shield, and by rather weak eddy currents that are uniformly distributed along the shield thickness (skin effect neglected). For these frequencies, the 2D model predicts a very poor shielding factor, because the flux barriers in the model do not exist in the real 3D perforated
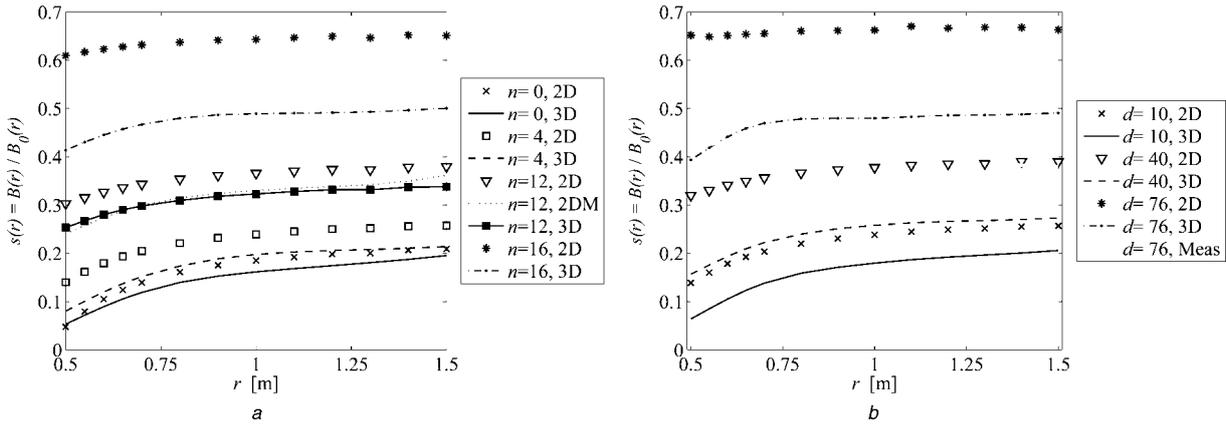
Figure 6 *For f = 10 kHz, shielding factor s(r) in the z = 0 plane*
a for several numbers of holes *n* with diameter 0.01 m
b for *n* = 2 holes with several hole diameters *d* in mm as a function of the position *r* in the target area
The results are obtained by unmodified 2D FEM (2D), modified 2D FEM (2DM), 3D FEM and measurements

shield. This means that the perforated shields for the given application can only be modelled accurately by the 3D model. However, it would be useful to determine an approximate 2D model and reach a compromise between accuracy and speed. A better correspondence between the 2D and 3D models could be achieved by introducing in the 2D model an equivalent air gap d_{eq}, obtained from reluctance considerations. It is emphasised that this approach is only valid if the field lines can be assumed to be parallel to the shield. To approximate the reluctance of the 3D shield with n_h holes along the circumference, we assume that there are n_h parallel flux paths with constant width b (see Fig. 1, flux along z-direction). The reluctance becomes

$$\mathcal{R} \approx \frac{1}{\mu} \frac{h_p}{t_p n_h b} \qquad (1)$$

This approximation overestimates the reluctance, because the average section available for the flux is larger than $t_p n_h b$.

In the 2D model, the reluctance of the shield consists of two contributions in series: the shield segments with high permeability and total height $h_p - n d_{eq}$, and the air gaps (with total height $n d_{eq}$) that separate the shield segments – see Fig. 2.

$$\mathcal{R} = \frac{1}{\mu} \frac{h_p - n d_{eq}}{t_p n_h (b + d)} + \frac{1}{\mu_0} \frac{n d_{eq}}{t_p n_h (b + d)} \qquad (2)$$

By expressing equality of both reluctances, the equivalent air gap can be determined

$$d_{eq} = \frac{h_p d}{n b (\mu_r - 1)} \qquad (3)$$

Furthermore, the conductivity should be modified, so that

the resistance seen by the eddy currents that flow in azimuthal direction are the same in the 3D and in the modified 2D models. The available section in 3D always has thickness t_p and a height that varies between b and $(b + d)$. The average section height for eddy currents is

$$h_{ec,avg} = \frac{(b + d)^2 - \pi d^2/4}{b + d} \qquad (4)$$

In the 2D model with gap diameter d_{eq}, the height of the section for the eddy currents is $b + d - d_{eq}$. The product of conductivity and available section is an indication for the resistance seen by the eddy currents. To obtain an equal resistance for eddy currents, an equivalent conductivity σ_{eq} is introduced in the modified 2D model

$$\sigma \frac{(b + d)^2 - \pi d^2/4}{b + d} = \sigma_{eq}(b + d - d_{eq}) \qquad (5)$$

$$\rightarrow \sigma_{eq} = \sigma \frac{(b + d)^2 - \pi d^2/4}{(b + d)(b + d - d_{eq})} \qquad (6)$$

For higher frequencies where skin effect is not negligible, the above low-frequency approximations for d_{eq} and σ_{eq} are not correct any more. The reason is that the modified conductivity in the above approximation also changes the penetration depth. As a result, the section for the eddy currents in the equivalent model is different from the one in the 3D model, because the current can penetrate inside the shield differently. This problem is tackled as follows. As in the high-frequency region, the shielding is caused almost completely by eddy currents, the section d_{eq} is changed so that the section of eddy currents is the same in both models, without changing the penetration depth. This means that the conductivity is not modified: $\sigma_{eq} = \sigma$. The

equivalent gap diameter becomes

$$\frac{(b+d)^2 - \pi d^2/4}{b+d} = (b + d - d_{eq}) \qquad (7)$$

$$\rightarrow d_{eq} = \frac{\pi d^2}{4(b+d)} \qquad (8)$$

This approximation does not take into account the increased path length of the eddy currents.

Introducing d_{eq} and σ_{eq}, instead of d and σ, in the 2D model yields a modified 2D model that behaves under certain conditions similarly to the 3D model, as verified in the next section.

2.5 Validation of the modified 2D FEM

As a function of the radial distance and at 100 Hz, the accuracy of the modified 2D (2DM) model can be seen in Fig. 5a for $n = 12$. The curve of the 2DM model (dashed line) is close to the corresponding curve of 3D FEM (with black square markers). The low-frequency approximations (3) and (6) of the equivalent diameter and conductivity seem to be a good approximation.

At 10 kHz, Fig. 6a also shows good correspondence between the 3D model and the 2DM model, using the high-frequency approximation (8) for the equivalent diameter.

For other diameters of d and the same two frequencies, Fig. 7a shows the average field in the target area as predicted by the 3D model. It illustrates the deterioration of the shielding as the hole diameter increases. Fig. 7b focuses on the difference between the 2DM and the 3D model, by showing the ratio $R_B = B_{avg,2DM}/B_{avg,3D}$. At 100 Hz and 10 kHz, the 2DM approximations deviate for most d-values by not more than 10%. The largest deviations are found for the largest d-values at 10 kHz: the 2DM model does not take into account the increased path length of the eddy currents, which results in higher eddy currents and better shielding efficiency. Fig. 7c shows the ratio of the equivalent diameter to the original one, in both the low-and the high-frequency approximations. Both approximations are completely different. As a result, unreliable results will occur in the frequency region around the 'switching frequency' where the equivalent d is switched from thelow-frequency approximation to the high-frequency approximation.

The results of the 2DM and the 3D FEM as a function of the frequency, as well as the behaviour of the 2DM at the switching frequency, are shown in Fig. 8. The switching frequency is chosen equal to the frequency where $\delta = t_p$. It will be shown hereafter that this choice is acceptable. Fig. 8 illustrates this frequency of 273 Hz by a vertical line. The predictions of the 2DM are shown using both the low-frequency and the high-frequency approximations in the whole frequency range. Evidently, the 2DM chooses the low-frequency
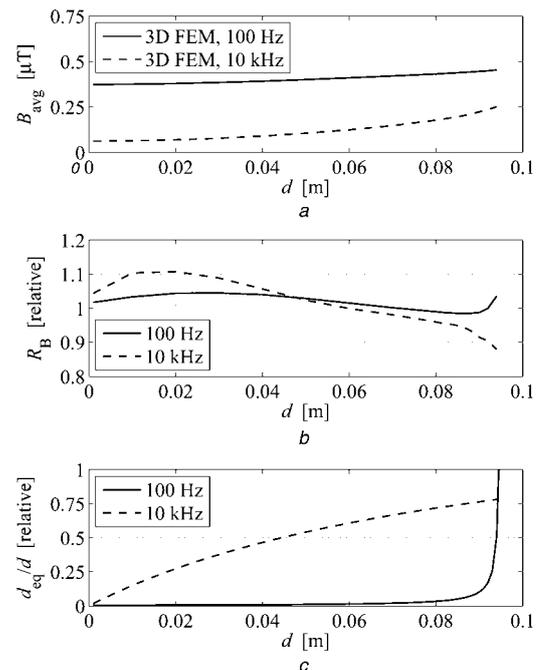

Figure 7 For $n = 2$

a average shielding predicted by the 3D FEM deteriorates if the hole diameter increases
b ratio between the average fields of the modified 2D FEM and the 3D FEM is close to one at 100 Hz and at 10 kHz
c the ratio of equivalent diameter to original diameter is different in the low-frequency approximation (at 100 Hz) and in the high-frequency approximation (at 10 kHz)

approximation for frequencies below the switching frequency, and the high-frequency approximation for higher frequencies. At the switching frequency, a small 'jump' of 9% is made, which is acceptable given the limited accuracy of this method
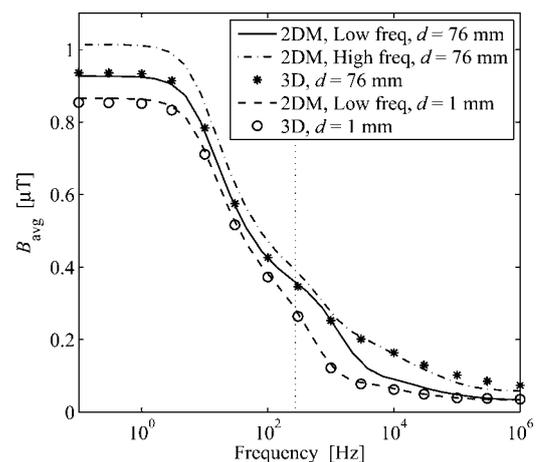

Figure 8 Average field obtained by the modified 2D FEM in low-frequency approximation and in high-frequency approximation for $n = 2$. For the hole diameter of 1 mm, the high-frequency approximation is not shown because it almost coincides with the low-frequency approximation. The switching between the high- and the low-frequency approximations is at the frequency 273 Hz where $\delta = t_p$ (vertical line)

and given the fact that the large diameter of 76 mm is almost a worst-case scenario. Between 0.1 Hz and 30 kHz, the difference between 2DM FEM and 3D FEM is always less than 10%. For small d, the accuracy is much better, and both the high- and the low-frequency approximations almost coincide. The curves in Fig. 8 as well as in Fig. 5a make it clear that the low-frequency approximation is useful up to 1 kHz. The high-frequency approximation is useful for frequencies higher than approximately 100 Hz. The switching should be between 100 Hz and 1 kHz.

We can conclude that the modified 2D model allows one to reach a compromise between accuracy and speed by means of using this fast 2D FEM model, instead of a slower 3D model for studying perforated shields. When considering another application, it may be necessary to modify (3), (6) and (8) depending on the field pattern and the shield geometry. The accuracy of the modified 2D FEM depends on the geometry of the application.

3 Method 1: fast design of a magnetic shield

The 2DM model can be used in an optimisation problem, in combination with a gradient-based minimisation algorithm. As an example, a numerical optimisation is carried out with the following objectives: best shielding factor and minimal volume of the shield. The parameters to optimise are the number n of holes in axial direction and the diameter d of the holes. As n is a discrete number, we carried out several optimisations of d at 10 kHz frequency using different values for n. The objective value is a weighted sum of the average field in the target area and the volume of the shield: $F(d, n) = 10^6 B_{avg,3D} + 2.2 \times 10^3 V_p$ and $C(d, n) = 10^6 B_{avg,2D} + 2.2 \times 10^3 V_p$, with

$$V_p = 2\pi r_p t_p \left(h_p - \frac{n}{b+d} \frac{\pi}{4} d^2 \right)$$

The choice of the weighting factor depends on the relative importance that is assigned to the field reduction, on the one hand, and to the volume, on the other hand. With the chosen weighting factors, the optimum was 0.085 m for $n = 2$. This value is compared with the optimum of the 3D FEM in the following section.

4 Method 2: accurate design of a magnetic shield

If an accurate study of 3D perforated shields is required, for the considered induction heating application, a 3D numerical model should be used. The computation time is reduced by using the thin-shell approach and by implementing a space mapping optimisation algorithm, which combines the fast unmodified 2D model and the accurate 3D model to find the optimum of the 3D model faster than conventional

optimisation algorithms. This algorithm [6] optimises several parameters by combining both the (unmodified) 2D FEM 'coarse model' C and the 3D FEM 'fine model' F and minimising a cost. The difference between the two models is taken into account by establishing a mapping function.

We explain this algorithm step by step for the same optimisation as in Section 3, because the version of aggressive space mapping (ASM) used in this study differs from the classical version explained in [6].

The classical ASM is explained based on Figs. 9a and 9b that show the fine and coarse objective functions and their gradients for $n = 2$, as a function of d, which is the only parameter to optimise. The point to find is the optimum of the fine model, denoted by d_f^*. The ASM starts by finding the optimum of the coarse objective function d_c^*, which is clearly different from the fine optimum d_f^*. The optimisation of the coarse model is done by a gradient-based algorithm. Second, in the resulting point d_c^*, the fine model is evaluated: $F(d_c^*)$. The third step is a crucial one, called parameter extraction. This means that a point has to be found in the coarse model, which corresponds to the point $F(d_c^*)$ in the fine model. In the classical ASM, this is the point where the function value of the coarse model is equal to $F(d_c^*)$. The parameter extraction yields the point d_1 where $C(d_1)$ has the *same*
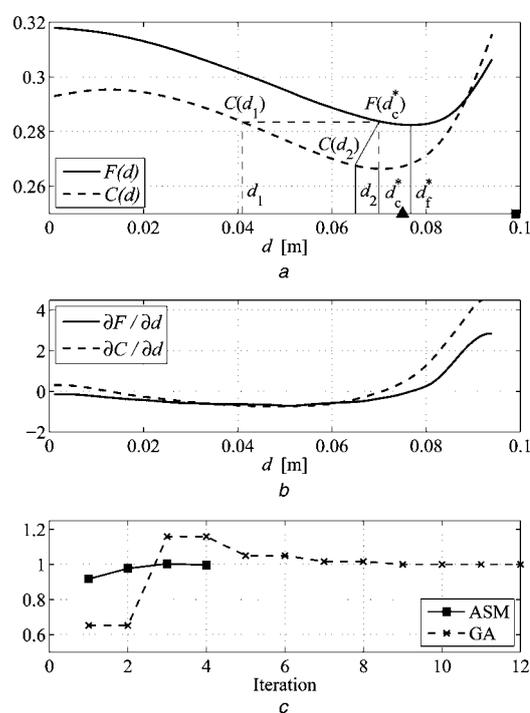
Figure 9 *Objective value and gradients of the fine and coarse objective functions F and C as a function of the hole diameter for n = 2 and convergence*

a Objective value of fine and coarse objective functions
b Gradients value of fine and coarse objective functions
c Convergence by showing the value of *d* relative to the optimum of 0.076 m for the aggressive space mapping (ASM) and gradient algorithm (GA)

function value as $F(d_c^*)$. In the fourth step, the ASM determines a new estimation of the optimum, based on the old estimation d_c^* and the point d_1. As in the coarse model d_1 is much smaller than the coarse optimum d_c^*, the ASM thinks that in the fine model, d_c^* is much smaller than the fine optimum to find. Consequently, the ASM will choose a new estimation for the optimal d that is much larger than the present one d_c^*: it chooses the point indicated by a black square in Fig. 9. The way to calculate the new estimation can be found in [6]. However, values for d where $d > h_p/n = 0.095$ for $n = 2$ are infeasible, so that the estimation of d will be reduced to its maximally allowed value. After finishing these steps in the initial iteration, the next iterations repeat Steps 2–4 until the optimum is found. However, as a result of the bad parameter extraction, the updated estimation of the optimum is worse than the previous one, so that the algorithm does not converge properly.

The version of ASM used in this study differs from the classical version explained in [6]: the parameter extraction is based on gradients of both $F(d)$ and $C(d)$, and not on their function values. The reason for this is the rather big difference in function values $C(d_c^*)$ and $F(d_f^*)$, where d_c^* and d_f^* are the optimal diameters in both models for a given number of holes. We repeat the algorithm from Step 2, starting again from d_c^*, and this time by applying the parameter extraction based on gradients. The parameter extraction now finds the point d_2 where $C(d_2)$ has the *same gradient* as $F(d_2)$. Fig. 9a shows that the distances $|d_2 d_c^*|$ and $|d_c^* d_f^*|$ are almost equal, so that in the next iteration, the algorithm will update the estimation to the point indicated by a black triangle, which is very close to the optimum d_f^* to be found.

For an optimisation at 10 kHz, the ASM finds the optimal solution after 4 evaluations of F and 55 evaluations of C, although the coarse optimum $d_c^* = 0.070$ m differs from the fine optimum $d_f^* = 0.076$ m. When optimising F using a gradient algorithm (GA), 12 evaluations are needed. As an evaluation of C is approximately 10 times faster than an evaluation of F, it is clear that space mapping is faster. The optimisations were carried out for $n = 2$, 4, 6 and 8. However, the objective function had an almost identical behaviour. We can conclude that it does not matter if the shield has a few big holes or many small holes if the total surface of the holes is equal. The optimised shield with $n = 2$ and $d = 76$ mm was experimentally tested; its shielding factor corresponds well with the simulations as can be seen for $f = 100$ Hz and 10 kHz, respectively in Fig. 5b and 6b. Fig. 3 shows $|B_z(r)|$ for 1 kHz. Fig. 9a shows that the optimum is global, but the space-mapping algorithm does not guarantee the finding of a global optimum, especially if the number of fine model evaluations is very small.

If the space mapping uses the modified 2D model, instead of the unmodified one, the optimisation uses only two evaluations of F and 22 evaluations of C. The first point where F is evaluated is the starting point (the optimum of the 2DM: 0.085 m),

and the second point is the fine optimum (where the derivative is so low that the optimisation stops). Although this optimisation is both fast and accurate, it may be less interesting because of the high development cost: both a 2D and a 3D model should be created, and the 2D model should be modified.

5 Conclusion

Perforations in a magnetic shield strongly deteriorate the shielding efficiency, both at low frequencies (where the shielding is caused by flux shunting) and at higher frequency (where shielding is mainly caused by eddy currents). Simulations show that the deterioration of the shielding by inserting holes is mainly determined by the volume of material that is removed. In other words, it is not important if the shield consists of many small holes, or just a few big holes. If the weight or the volume of shield material is important, it is possible to find an optimal hole diameter that results in good shielding efficiency and low weight.

The application with perforated shields is modelled in two ways. The first way consists in establishing a modified 2D model by means of an equivalent air gap and conductivity, which better approximates the 3D application and gives results closer to the 3D model. This method is easy-to-implement and fast, but its accuracy strongly depends on the geometry of the application. For low frequencies where skin effect is negligible (penetration depth larger than shield thickness), the modifications are different than for high frequencies where skin effect occurs. It is shown that the modified 2D model deviates less than 10% from the 3D FEM for a (large) hole diameter of 76 mm, and for frequencies between 0.1 Hz and 30 kHz. Also for other hole diameters, the deviation is usually less than 10%. The second way is a 3D FEM which is, thanks to the thin-shell formulation, faster than a conventional 3D FEM.

To optimise the hole diameter and the number of holes in a time-efficient way, two methods are presented. The first method uses the modified 2D FEM. The second method uses the 3D FEM with thin-shell approximation and a space-mapping algorithm for optimisation. For the considered induction heating application, simulations and experiments show good correspondence, even with a linearised material model (constant permeability). Despite the large approximations made in the modified 2D FEM, Method 1 yields acceptable results concerning the shielding, although it is evidently less accurate than Method 2. For other applications, the influence of the shield geometry on the field intensity should be checked. A non-linear model should be used if certain regions of the shield are in the Rayleigh zone or the saturated zone.

6 Acknowledgments

7 References

[1] SERGEANT P., DUPRÉ L., MELKEBEEK J.: 'Active and passive magnetic shielding for stray field reduction of an induction heater with axial flux', *IEE Proc. Electr. Power Appl.*, 2005, **152**, (5), pp. 1359–1364

[2] HAHN A., KOST A., JÄNICKE L., MIETHNER K.: 'Fields and shielding by eddy currents in perforated boxes', *Int. J. Appl. Electromagn. Mech.*, 2003, **17**, pp. 31–43

[3] DI X., MOSES A.J., ANDERSON P.: 'Measured and computed effect of holes on low-frequency magnetic shielding performance of electrical steel sheet', *IEEE Trans. Magn.*, 2006, **42**, (10), pp. 3527–3529

[4] ROBINSON M.P., BENSON T.M., CHRISTOPOULOS C., ET AL.: 'Analytical formulation for the shielding effectiveness of enclosures with apertures', *IEEE Trans. Electromagn. Comput.*, 1998, **40**, (3), pp. 240–248

[5] SERGEANT P., DUPRÉ L., MELKEBEEK J.: 'Space mapping method for the design of passive shields', *J. Appl. Phys.*, 2006, **99**, (8), 08H901

[6] BANDLER J.W., CHENG Q.S.S., DAKROURY S.A., ET AL.: 'Space mapping: the state of the art', *IEEE Trans. Microw. Theory Tech.*, 2004, **52**, (1), pp. 337–361

[7] SILVESTER P.P., FERRARI R.L.: 'Finite elements for electrical engineers' (Cambridge University Press, Cambridge, 1990)

[8] SERGEANT P., DUPRÉ L., DE WULF M., MELKEBEEK J.: 'Optimizing active and passive magnetic shields in induction heating by a Genetic Algorithm', *IEEE Trans. Magn.*, 2003, **39**, (6), pp. 3486–3496

[9] GEUZAINE C., DULAR P., LEGROS W.: 'Dual formulations for the modeling of thin electromagnetic shells using edge elements', *IEEE Trans. Magn.*, 2000, **36**, (4), pp. 799–803

[10] SERGEANT P., ZUCCA M., DUPRÉ L., ROCCATO P.: 'Magnetic shielding of a cylindrical shield in nonlinear hysteretic material', *IEEE Trans. Magn.*, 2006, **42**, (10), pp. 3189–3191

[11] International Commission on Non-Ionizing Radiation Protection: 'Guidelines for limiting exposure to time-varying electric, magnetic, and electromagnetic fields (up to 300 GHz)', *Health Phys.*, 1998, **74**, (4), pp. 494–522